Baranwal *et al. Nano Convergence (2017) 4:26*
DOI 10.1186/s40580-017-0120-3

Nano Convergence

RESEARCH Open Access

Lead-free perovskite solar cells using Sb and Bi-based $A_3B_2X_9$ and A_3BX_6 crystals with normal and inverse cell structures

Ajay Kumar Baranwal[1*], Hideaki Masutani[1], Hidetaka Sugita[1], Hiroyuki Kanda[1], Shusaku Kanaya[1], Naoyuki Shibayama[1], Yoshitaka Sanehira[2], Masashi Ikegami[2], Youhei Numata[2], Kouji Yamada[3], Tsutomu Miyasaka[2], Tomokazu Umeyama[4], Hiroshi Imahori[4] and Seigo Ito[1*]

Abstract

Research of $CH_3NH_3PbI_3$ perovskite solar cells had significant attention as the candidate of new future energy. Due to the toxicity, however, lead (Pb) free photon harvesting layer should be discovered to replace the present $CH_3NH_3PbI_3$ perovskite. In place of lead, we have tried antimony (Sb) and bismuth (Bi) with organic and metal monovalent cations ($CH_3NH_3^+$, Ag^+ and Cu^+). Therefore, in this work, lead-free photo-absorber layers of $(CH_3NH_3)_3Bi_2I_9$, $(CH_3NH_3)_3Sb_2I_9$, $(CH_3NH_3)_3SbBiI_9$, Ag_3BiI_6, $Ag_3BiI_3(SCN)_3$ and Cu_3BiI_6 were processed by solution deposition way to be solar cells. About the structure of solar cells, we have compared the normal (n-i-p: TiO_2-perovskite-spiro OMeTAD) and inverted (p-i-n: NiO-perovskite-PCBM) structures. The normal (n-i-p)-structured solar cells performed better conversion efficiencies, basically. But, these environmental friendly photon absorber layers showed the uneven surface morphology with a particular grow pattern depend on the substrate (TiO_2 or NiO). We have considered that the unevenness of surface morphology can deteriorate the photovoltaic performance and can hinder future prospect of these lead-free photon harvesting layers. However, we found new interesting finding about the progress of devices by the interface of NiO/Sb^{3+} and TiO_2/Cu_3BiI_6, which should be addressed in the future study.

Keywords: Lead-free perovskite, Solar cells, Antimony, Bismuth

1 Introduction

Recent advancements of organic–inorganic perovskite ($CH_3NH_3PbI_3$) thin-film solar cells, which can be fabricated by economical-promising solution process, have marked significant achievements of photoconversion efficiency (PCE) from the initial efficiency of 3.8% to over 22% [1–3]. The PCE progress has been realized due to the excellent ability of $CH_3NH_3PbI_3$ about light harvesting, charge separation and charge transportation. These excellent properties also realize to fabricate perovskite solar cells in different structural designs as normal (n-i-p) mesoscopic and inverted (p-i-n) planar configurations. However, the working instability had been a profound problem [4–7]. Moreover, the toxicity of lead (Pb) shows big impact on the environment and human being, and then, the quest for such lead-free thin film solar cell has been highly demanded [8, 9]. The first lead-free perovskite solar cells were initially fabricated with the substitution of lead to tin (Sn) for the mesoscopic structure solar cells as <FTO glass/cp-TiO_2/$CH_3NH_3SnI_3$/Spiro-OMeTAD/Au> [10, 11]. A moderate PCE of 6% was reported, but the rapid oxidation of Sn^{2+} to be Sn^{4+} at the ambient condition arised concern. Afterward, however, it was found that tin cation shows higher toxicity than lead [12]. Hence, another elements have been considered for the further ongoing lead-free solar cells.

In order to substitute the Pb, another potential, germanium (Ge^{2+}) cation was implemented into the organo-metal-halide crystal as a harvesting layer, which has the same oxidation state and lower electronegativity and

---

*Correspondence: ajaybarn@gmail.com; itou@eng.u-hyogo.ac.jp
[1] Department of Materials and Synchrotron Radiation Engineering, Graduate School of Engineering, University of Hyogo, 2167 Shosha, Himeji, Hyogo 671-2280, Japan
Full list of author information is available at the end of the article

resulted in 0.2% PCE [13]. As another divalent, earth abundant and non-toxic element, copper cation was utilized in mesoscopic perovskite solar cell structure with $(CH_3NH_3)_2CuCl_xBr_y$ as a photon harvesting layer [14]. The low PCE of 0.017% was observed due to the low absorption coefficients, the high effective mass of holes and the low intrinsic conductivity of the employed perovskite layer.

The other viable opinion towards lead cation (Pb^{2+}) substitution is adaptation of heterovalent (not divalent) cation into the organic-metal-halide crystals. These substitutions have to follow charge neutrality and can alter perovskite structure (ABX_3) to another crystal (A: organic ion; B: metal ion; X: halide ion). Recently, trivalent cations of antimony (Sb) and bismuth (Bi) based organic-metal-halide crystals ($A_3B_2X_9$ or A_3BX_6) got significant interest as a photon harvesting layer due to their environmentally friendly nature and available inactive outer shell s orbital [15, 16]. Öz et al. proposed $(CH_3NH_3)_3Bi_2I_9$ based inverted solar cells as <ITO/PEDOT:PSS/$(CH_3NH_3)_3Bi_2I_9$/PCBM/Ca/Al. However, the energy mismatch limited the charge extraction, resulting in the low PCE to 0.07%. Hebig et al. proposed <ITO/PEDOT:PSS/$(CH_3NH_3)_3Sb_2I_9$)/PCBM/ZnO/Al> structures and reported 0.49% PCE [15, 16]. The trivalent bismuth (Bi^{3+}) has utilized for the fabrication of $(CH_3NH_3)_3Bi_2I_9$ based organic-metal-halide layer, which showed optimal absorption coefficient [17, 18]. This Bi-based organic-metal-halide solar cells were reported 0.33% of the low PCE, which was limited by its high exciton binding energy of 300 meV. It was founded that the morphology of $(CH_3NH_3)_3Bi_2I_9$ was changed by the selection of electron transporting layers (ETL), and that the small amount addition of NMP (*N*-methyl-2-pyrrolidone) solvent could also attain to grow uniform surface morphology [18, 19].

In order to improve the Bi-based A_3BX_6-structured solar cells, recently, Ag and Cs were composed as A-site monovalent cations to be Cs_2AgBiX_6 structure, due to better optical and electrical properties and its ambient stability [20–23]. The substitution of methylammonium ion with silver can extend the dimension of all inorganic active material maintaining its 3d structure, which can be more suitable for photo harvesting due to its uniform nature. Ag found application in various structural compounds including $AgBiI_4$ and $(CH_3NH_3)_2AgBiBr_6$ although, only optical properties are established and the PCE is yet to be demonstrated [24, 25]. Moreover, the Chemical materials Evaluation and REserarch BAse (CEREBA) reported the incorporation of the silver based A-site cation by replacing the methylammonium ($CH_3NH_3^+$) ion preserving the Bi and iodine (Ag_3BiI_6) and reported 4.3% PCE [23]. Hence, it can be assumed that the Ag–Bi based photo absorber can perform the lead free organo-metal-halide solar cells with better PCE.

In order to improve the photovoltaics of lead free $A_3B_2X_9$ and A_3BX_6 solar cells, the further morphological and structural study of Sb and Bi-based metal-halide layers and the effect on PCE should be studied. In this study, we have tried $A_3B_2X_9$ and A_3BX_6-structured crystals for the photo absorber layers of solar cells with several combinations of A site cations ($CH_3NH_3^+$, Ag^+ and Cu^+) and B site cations (Bi^{3+} and Sb^{3+}), which were $(CH_3NH_3)_3Bi_2I_9$, $(CH_3NH_3)_3Sb_2I_9$, $(CH_3NH_3)_3SbBiI_9$, Ag_3BiI_6, $Ag_3BiI_3(SCN)_3$ and Cu_3BiI_6. The crystal configurations of $A_3B_2X_9$ and A_3BX_6 were tried to be controlled by the amount of elements in the solutions of source materials. These crystal layers were implemented in normal (n-i-p) and inverted (p-i-n) solar cell architectures (Fig. 1): the normal mesoscopic solar cell <FTO glass/cp TiO_2/mp TiO_2/(Pb-free $A_3B_2X_9$ and A_3BX_6 layer)/spiro-OMeTAD/Au> and the inverted structure <FTO glass/NiO layer/(Pb-free $A_3B_2X_9$ and A_3BX_6 layer)/PCBM/BCP/Ag>. It was confirmed that the adjacent substrate to $A_3B_2X_9$ crystal (TiO_2 electron transporting layer (ETL) and NiO hole transporting layer (HTL)) affected on the lead-free $A_3B_2X_9$ and A_3BX_6 morphology and its effect on PCE are studied.

2 Results and discussion

2.1 $A_3B_2X_9$ crystals with methyl ammonium cation for the A site

The XRD patterns of $(CH_3NH_3)_3Bi_2I_9$, $(CH_3NH_3)_3Sb_2I_9$, and $(CH_3NH_3)_3SbBiI_9$ thin films are similar and possesses the strong preferential growth in c axis direction (Fig. 2a). The observed XRD peaks of thin $(CH_3NH_3)_3Bi_2I_9$ film at 8.16, 16.34 and 24.62 are well matched to the literature and correspond to the indexed planes (002), (004) and (006) respectively in a $P6_3/mmc$ hexagonal space group where preferential growth direction is in c axis direction [15]. The observed peak of $(CH_3NH_3)_3Sb_2I_9$ film at 8.22, 16.54, 24.88 and 50.98 could be indexed by planes (001), (002), (003) and (402) respectively in $P6_3/mmc$ hexagonal space group and possesses the strong preferential growth in c axis direction similar to the $(CH_3NH_3)_3Bi_2I_9$ film [16]. The XRD pattern of $(CH_3NH_3)_3SbBiI_9$ film containing Bi and Sb also shows preference to have the same c axis orientation growth. Due to the multi cation at B site in the crystal, we could not define the exact element at each position. Hence, we should not put the exact index at the peaks. The details analysis is ongoing for the next publication as the future works.

Figure 2b shows UV–vis spectra and photographs of $(CH_3NH_3)_3Bi_2I_9$, $(CH_3NH_3)_3Sb_2I_9$, and $(CH_3NH_3)_3SbBiI_9$ thin films. The $(CH_3NH_3)_3Bi_2I_9$ film absorbs with the peak appearing around 500 nm. On the other hand, The

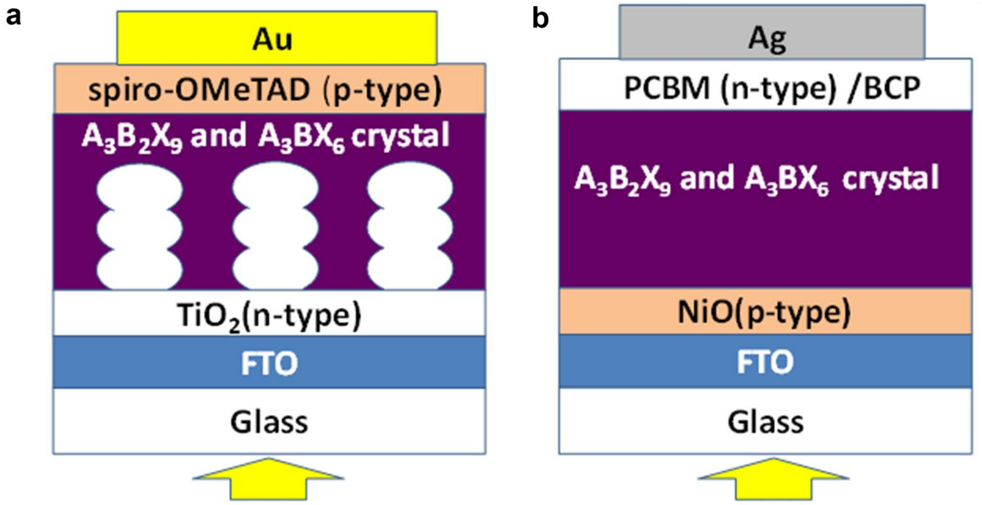

Fig. 1 Structures of fabricated solution processed lead-free $A_3B_2X_9$ and A_3BX_6 crystal (A: monovalent cation; B: trivalent cation; X: halogen anion) solar cells: normal mesoscopic (n-i-p) (**a**) and inverted planar (p-i-n) (**b**) structures

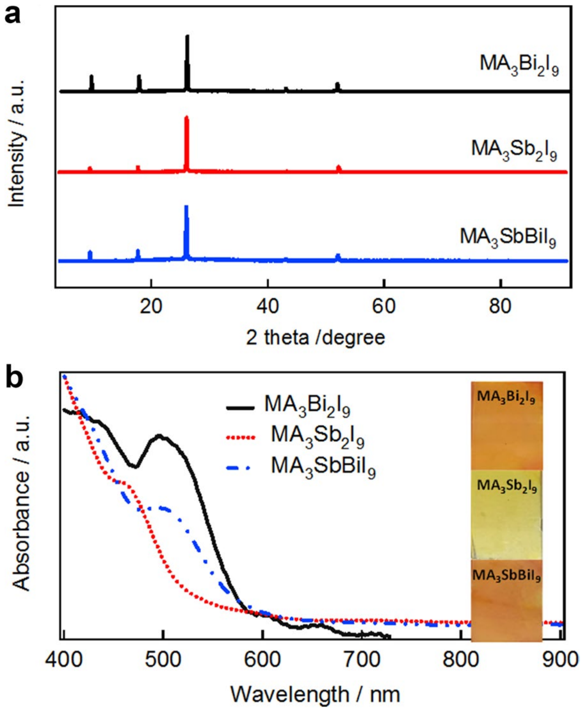

Fig. 2 XRD patterns (**a**) and UV–vis absorption spectra (**b**) of grown solution processed $(CH_3NH_3)_3Bi_2I_9$, $(CH_3NH_3)_3Sb_2I_9$ and $(CH_3NH_3)_3SbBiI_9$ films on a glass substrate. The insets were the pictures of $(CH_3NH_3)_3Bi_2I_9$, $(CH_3NH_3)_3Sb_2I_9$ and $(CH_3NH_3)_3SbBiI_9$ films

UV–vis spectrum of $(CH_3NH_3)_3Sb_2I_9$ shows a shoulder peak around 460 nm and no clear peak. The casted $(CH_3NH_3)_3SbBiI_9$ film shows higher absorption around 500 nm than $(CH_3NH_3)_3Bi_2I_9$ and $(CH_3NH_3)_3Sb_2I_9$ films. The exact absorption coefficients were not shown in the figure due to the inhomogeneous structures of films, which will be shown later.

The $(CH_3NH_3)_3Bi_2I_9$, $(CH_3NH_3)_3Sb_2I_9$, and $(CH_3NH_3)_3SbBiI_9$ layers processed on different substrates (TiO_2 or NiO) were observed with scanning electron microscopy (SEM) images (Fig. 3). Due to the crystal structures with hexagonal space group detected by XRD (Fig. 2a), the morphologies became also hexagonal shapes, basically. The $(CH_3NH_3)_3Bi_2I_9$ film growth morphology on TiO_2 layer is hexagonal (Fig. 3a), but were irregular hexagon and star shape on NiO film (Fig. 3b). Apparently, this observed variation of morphology pattern is attributed to the interface between metal oxides (TiO_2 and/or NiO) and $A_3B_2X_9$ organic-metal-halide crystals. On the other hand, the $(CH_3NH_3)_3Sb_2I_9$ (Fig. 3c, d) crystals were hexagonal simply, irrespective of substrate (TiO_2 and/or NiO). Additionally, on the NiO substrate, the appearing irregular hexagon shows its polycrystalline nature. About the $(CH_3NH_3)_3SbBiI_9$ film (Fig. 3e, f), these observed SEM images provide the information of the surface coverage, suggesting polycrystalline growth of hexagonal and irregular hexagonal in nature. Essentially, the inhomogeneity is involved in the growth of film, and the homogeneous surface coverage is difficult. This characteristics may be attributed to the poor PCE and with polycrystalline growth nature [26].

Figure 4 shows the SEM images of $(CH_3NH_3)_3Bi_2I_9$, $(CH_3NH_3)_3Sb_2I_9$, and $(CH_3NH_3)_3SbBiI_9$ crystals casted on TiO_2 and NiO substrates for the elemental distribution by EDX analysis. In order to reduce the electron charge accumulation on the surface during the EDX

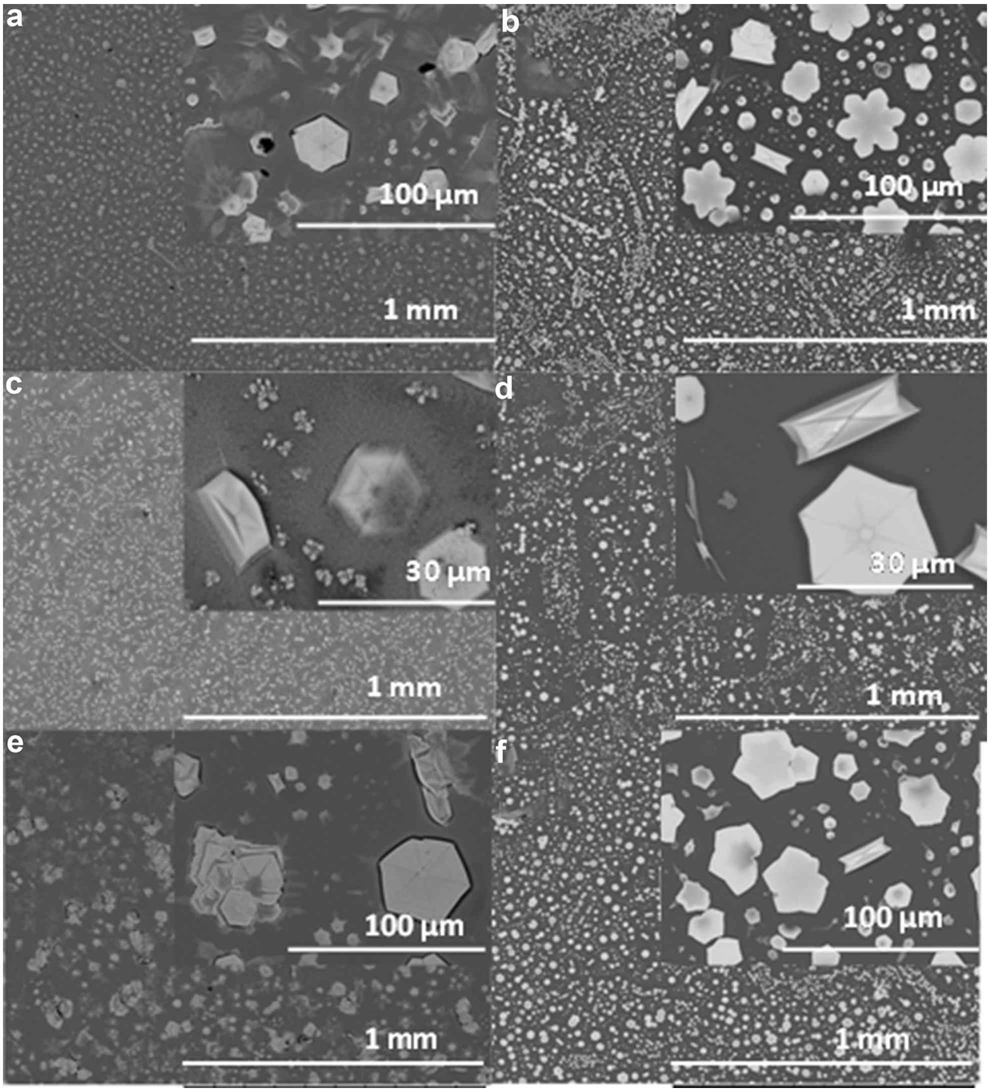

Fig. 3 SEM images of $A_3B_2X_9$ films [$(CH_3NH_3)_3Bi_2I_9$: (**a**, **b**); $(CH_3NH_3)_3Sb_2I_9$: (**c**, **d**); $(CH_3NH_3)_3SbBiI_9$: (**e**, **f**)] grown on different substrates [TiO_2: (**a**, **c**, **e**); NiO: (**b**, **d**, **f**)]

measurements, the gold (Au) thin layer was deposited by sputtering system beforehand. Hence the component contribution from Au was observed. The sum of all elemental contribution was set to be 100. The points of elemental analysis were chosen at various particular spot locations and are numbered in Fig. 4. The results of elemental analysis are summarized in Tables 1, 2, 3, 4, 5, 6, which are projected by the numbers in Fig. 4. About $(CH_3NH_3)_3Bi_2I_9$ film elemental analysis on TiO_2 substrates (Fig. 4a, Table 1), the small amounts of Bi and I out of grain were observed (points 4 and 5). The points on grain (point 1, 2, and 3) show the large amount of Bi and I than those out of grain (points 4 and 5). Hence, It can be confirmed that there was also the thin layer of $(CH_3NH_3)_3SbBiI_9$ at the points out of the large grain. The ratios of I/Bi at the points 1, 2, 3, 4, and 5 in Fig. 4a were 4.21, 3.91, 3.76, 4.08 and 4.25, respectively. Thinking about the I/Bi stoichiometry ratio (= 4.5) in the $(CH_3NH_3)_3Bi_2I_9$ crystal, the results of EDX show the reduction of iodide element in the material. Although Bi was distributed on all points of the TiO_2 surface (Table 1), there are missing points of Bi on NiO layer (at the points 2 and 3 in Table 2). The points 2 and 3 out of grain on NiO may possess only CH_3NH_3I. The ratios of I/Bi at the points 1, 4, and 5 in Fig. 4b and Table 2 are 4.92, 4.13, and 4.02, respectively, which are larger than those of grains in Fig. 4a and Table 1. Possibly, the solution of $(CH_3NH_3)_3Bi_2I_9$ was repelled from the surface of NiO and crystallized on NiO close to the stoichiometry ratio. About $(CH_3NH_3)_3Sb_2I_9$, it was surprising that

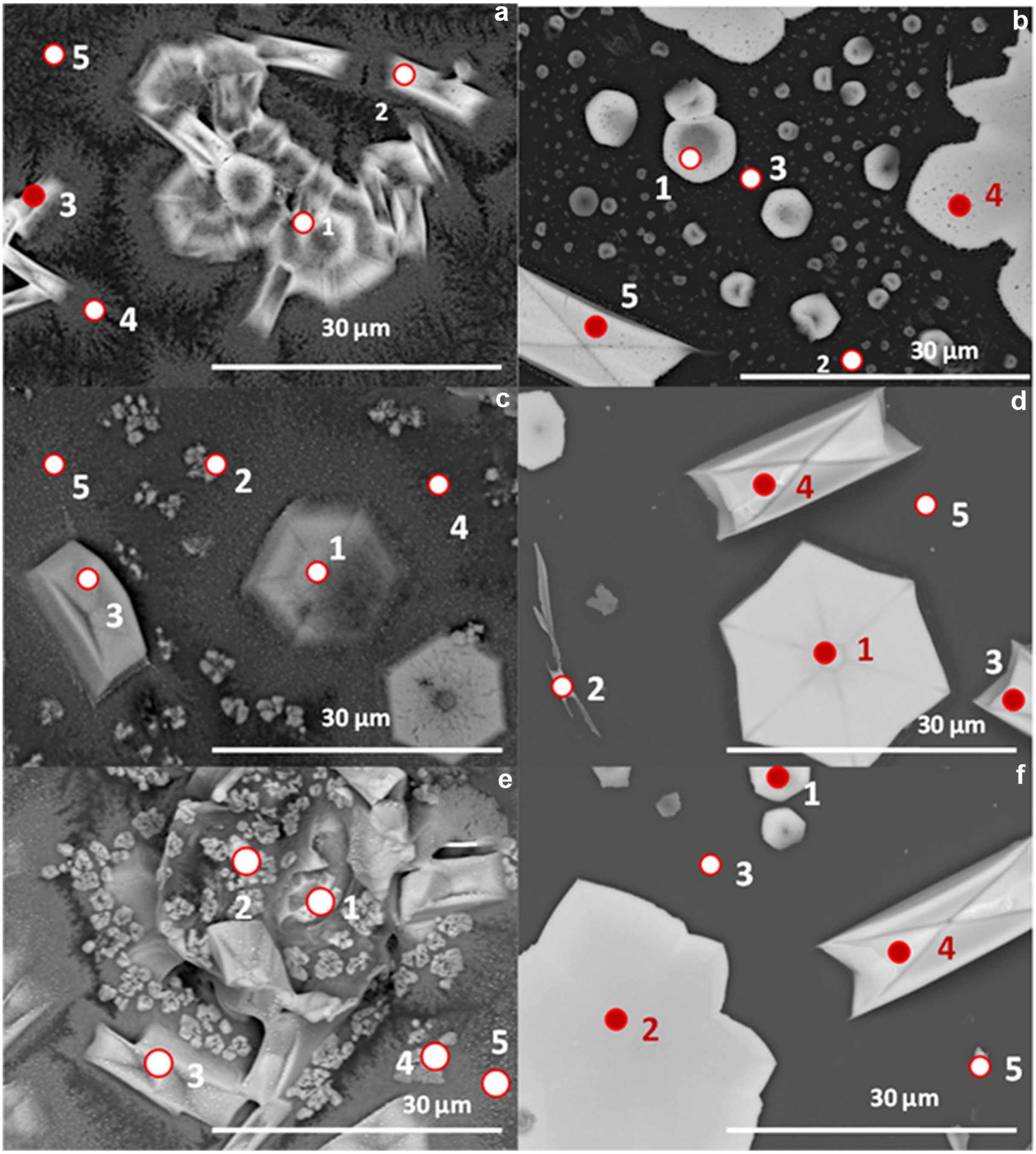

Fig. 4 SEM images observed for elemental analysis of $A_3B_2X_9$ films [$(CH_3NH_3)_3Bi_2I_9$: (**a**, **b**); $(CH_3NH_3)_3Sb_2I_9$: (**c**, **d**); $(CH_3NH_3)_3SbBiI_9$: (**e**, **f**)] grown on different substrates [TiO_2: (**a**, **c**, **e**); NiO: (**b**, **d**, **f**)]. The marked spots indicate the positions of elemental analysis, which are related to the results shown in Tables 1, 2, 3, 4, 5, and 6

there are missing points of Sb not only on NiO, but also on TiO_2 (Fig. 4c, d, Tables 3, 4). Therefore, the anchoring strength of Sb on to the oxides (TiO_2 or NiO) would be weaker than that of Bi. The elemental ratios (I/Sb) of crystals were 6.17 and 4.79 on TiO_2 (at the points 1 and 3 in Fig. 4c and Table 3) and 3.98, 3.65 and 4.03 on NiO (at the points 1, 3 and 4 in Fig. 4d and Table 4), respectively. The reason was not clear, but the elemental ratios (I/Sb) of crystals were higher on TiO_2 than NiO. About $(CH_3NH_3)_3SbBiI_9$ (Fig. 4e, f, Tables 5, 6), Bi was not observed out of the crystal as $(CH_3NH_3)_3Sb_2I_9$ (Fig. 4c, d, Tables 3, 4), which was predicted by the weak anchoring

Table 1 Elemental distribution (atomic %) of the individual elements observed on particular spot on $(CH_3NH_3)_3Bi_2I_9/TiO_2$ film shown in Fig. 4a

Spot	Bismuth	Iodine	Titanium	Gold
Point 1	10.00	42.10	45.55	2.72
Point 2	12.87	50.35	34.17	2.59
Point 3	17.25	64.87	14.49	3.11
Point 4	6.32	25.79	64.17	3.29
Point 5	2.79	11.86	80.89	4.02

Table 2 Elemental distribution (atomic %) of the individual elements observed on a particular spot on $(CH_3NH_3)_3Bi_2I_9$/NiO film shown in Fig. 4b

Spot	Bismuth	Iodine	Nickel	Gold
Point 1	13.92	68.52	10.88	6.95
Point 2	0.00	11.14	46.54	42.31
Point 3	0.00	12.25	45.62	42.12
Point 4	18.07	74.56	2.33	4.64
Point 5	19.01	76.55	0.92	3.29

Table 3 Elemental distribution (atomic %) of the individual elements observed on particular spot on $(CH_3NH_3)_3Sb_2I_9/TiO_2$ film shown in Fig. 4c

Spot	Antimony	Iodine	Titanium	Gold
Point 1	7.71	47.59	38.97	5.71
Point 2	0.00	26.17	66.96	6.86
Point 3	13.06	62.55	22.25	2.12
Point 4	0.00	15.55	78.85	5.37
Point 5	0.00	8.95	89.17	1.66

Table 4 Elemental distribution (atomic %) of the individual elements observed on a particular spot on $(CH_3NH_3)_3Sb_2I_9$/NiO substrate shown in Fig. 4d

Spot	Antimony	Iodine	Nickel	Gold
Point 1	19.54	77.83	0.26	2.35
Point 2	0.00	6.83	43.44	49.72
Point 3	20.26	73.91	0.71	5.10
Point 4	19.64	79.22	0.20	0.93
Point 5	0.00	3.84	44.04	52.11

strength between Sb and metal oxides as above. Although the material ratio in the solution of $(CH_3NH_3)_3SbBiI_9$ was in the stoichiometry, the elemental ratio of Sb/Bi was changed very much to the crystals, which would be due to the segregation to $(CH_3NH_3)_3SbI_9$ and $(CH_3NH_3)_3BiI_9$.

Table 5 Elemental distribution (atomic %) of the individual elements observed on $(CH_3NH_3)_3SbBiI_9/TiO_2$ substrate shown in Fig. 4e

Spot	Antimony	Bismuth	Iodine	Titanium	Gold
Point 1	2.70	3.11	23.86	68.98	1.32
Point 2	11.18	8.04	74.57	3.18	3.00
Point 3	9.09	7.42	65.20	11.73	6.23
Point 4	0.00	3.01	29.55	60.94	6.35
Point 5	0.00	3.76	27.73	65.99	2.50

Table 6 Elemental distribution (atomic %) of the individual elements observed on $(CH_3NH_3)_3SbBiI_9$/NiO substrate shown in Fig. 4f

Spot	Antimony	Bismuth	Iodine	Nickel	Gold
Point 1	6.36	8.85	74.85	2.55	7.36
Point 2	1.32	8.68	71.86	5.81	11.76
Point 3	0.00	0.00	3.58	38.82	57.58
Point 4	9.54	9.71	75.48	0.12	5.13
Point 5	3.83	9.61	60.83	7.86	17.85

The elemental ratios (I/(Sb + Bi)) of $(CH_3NH_3)_3SbBiI_9$ crystals were 4.11, 3.92, and 3.95 on TiO_2 (at points 1, 2, and 3 in Fig. 4e and Table 5) and 4.92, 7186, 3.92, and 4.52 on NiO (at points 1, 2, 4 and 5 in Fig. 4f and Table 6), respectively. The large variation of elemental ratio [I/(Sb + Bi)] would be attributed to the crystal segregations. Anyway, the SEM–EDX analysis suggests the nonuniformity of the crystals of $(CH_3NH_3)_3Bi_2I_9$, $(CH_3NH_3)_3Sb_2I_9$, and $(CH_3NH_3)_3SbBiI_9$. These all results are in contrast to the lab scale established $CH_3NH_3PbI_3$ perovskite-based solar cells where high efficiencies are achieved with uniform and pin hole free surface morphology [27, 28].

Figure 5 shows the photo I–V characteristics of solar cells with best PCE using the lead-free photo absorbing materials ($(CH_3NH_3)_3Bi_2I_9$, $(CH_3NH_3)_3Sb_2I_9$, and $(CH_3NH_3)_3SbBiI_9$) with different structure (n-i-p and p-i-n, in Fig. 1), measured under the simulated sun light (AM 1.5, 100 mW cm^{-2}). The observed PCE parameters are summerized in Table 7 and are significantly lower than the standard perovskite solar cells using $CH_3NH_3PbI_3$ [1–3], which would be attributed to the uneven surface morphology of lead free perovskite solar cells. Basically, the cells using porous-TiO_2 electrode gave better *FF*s, which is due to the prohibition of short circuiting by porous TiO_2 layer [29]. Actually, the cells without $A_3B_2I_9$ conformal layers on porous TiO_2 [$(CH_3NH_3)_3Sb_2I_9$ (Table 3) and $(CH_3NH_3)_3SbBiI_9$ (Table 5)] also provide better *FF*s.

On the other hand, the cells using NiO provide small *FF*s. Specially, the cells using $(CH_3NH_3)_3Bi_2I_9$ on NiO performed the short circuitting (Fig. 5b, Table 2). However, in spite of the missing points of $(CH_3NH_3)_3Sb_2I_9$ and $(CH_3NH_3)_3SbBiI_9$ on NiO (Tables 4, 6), the I–V curves in Fig. 5d and f show *FF*s over 0.3. The prohibition of short circuiting would be due to the slight presence of Sb^{3+} on NiO surface, which was not detected by the EDX analysis. It was interesting that the hysteresis of $A_3B_2X_9$ solar cells on NiO layer were smaller than those on TiO_2 layer, as $CH_3NH_3PbI_3$ solar cells [30].

2.2 A_3BX_6 crystals with Ag or Cu cation for the A site

Copper and silver are non-toxic material and especially, Cu^+ is a cheap and earth abundant one. The structure of A_3BX_6 was regulated by the ratio of elemental materials in the DMSO solution. Hence, CuI and BiI_3 were mixed in 3:1 molar ratio to be Cu_3BiI_6. AgI and BiI_3 were mixed in 3:1 molar ratio to be Ag_3BiI_6. In case of $Ag_3BiI_3(SCN)_3$, AgSCN and BiI_3 were mixed in 3:1 molar ratio. The XRD patterns of Ag_3BiI_6, $Ag_3BiI_3(SCN)_3$ and Cu_3BiI_6 as casted films are shown in Fig. 6a. The film made by Ag_3BiI_6 signifies the trigonal structure with $R\ \bar{3}\ m$ space group [31]. The space group determination of relatively new materials $Ag_3BiI_3(SCN)_3$ and Cu_3BiI_6 could not be realized. Now, we are analyzing the exact crystal structures of $Ag_3BiI_3(SCN)_3$ and Cu_3BiI_6 as the further research works. Figure 6b shows the UV–vis absorption spectra observed. The Ag_3BiI_6 and Cu_3BiI_6 films show higher absorption than the $Ag_3BiI_3(SCN)_3$ one. Due to the absorbance onset of Ag_3BiI_6 and Cu_3BiI_6 at around 680 nm, the films were dark brown. On the other hand, $Ag_3BiI_3(SCN)_3$ film was pale yellowish. The difference of Ag_3BiI_6 and Cu_3BiI_6 were the variation of spectra at around 580 nm. The exact absorption coefficients were not shown in the figure due to the inhomogeneous structures of films, which will be shown later.

Figure 7 shows the surface morphologies of Ag_3BiI_6, $Ag_3BiI_3(SCN)_3$ and Cu_3BiI_6 films on porous-TiO_2 and planer-NiO substrates which were observed by the SEM. Although the Ag_3BiI_6 films seems to be uniform observed by eyes, the nanoscale morphology in this SEM image scaled at 1 μm was relatively uniform (Fig. 7a). It was noticed that there were 1 μm-sized small grains of Ag_3BiI_6 on porous-TiO_2 (Fig. 7a). However, Ag_3BiI_6 on planer NiO became the flakey layer with cracks, and exact crystals were not observed in the SEM image (Fig. 7b). For the other silver cation and mixed anion based $Ag_3BiI_3(SCN)_3$ film, the SEM image with 10 μm scale shows the leaf-like crystal pattern on porous-TiO_2 substrate and the grain structure on planer-NiO substrate with space between the crystals as the non-uniform substrate coverage resulting in the limitation in photon harvesting and charge collection (Fig. 7c, d). The morphologies of Cu_3BiI_6 were small grains with around 0.1–0.5 μm which were dispersed homogeneously on porous-TiO_2 and planer-NiO substrates (Fig. 7e, f).

The individual elemental distribution (EDX analysis) involved of surface morphology of Ag_3BiI_6, $Ag_3BiI_3(SCN)_3$ and Cu_3BiI_6 films are shown in Tables 8, 9, 10, 11, 12 and 13. The analyses spots were chosen randomly and are shown on its SEM images in Fig. 7. Although A_3BX_6 crystals of Ag_3BiI_6, $Ag_3BiI_3(SCN)_3$ and Cu_3BiI_6 distributed relatively homogeneously than $A_3B_2X_9$ ones using $CH_3NH_3^+$ cations (Fig. 3 and Tables 1, 2, 3, 4, 5, 6), still the materials were dispersed with inhomogeneity about the elemental ratio (Tables 8, 9, 10, 11, 12, 13). It can be noticed that the amount of Bi was smaller than A site monovalent cations (Ag^+ and Cu^+). Specially, it was prominent that the amount of Ag^+ was quite higher than that of Bi^{3+}, which should be improved for the further progress.

The photo I–V characteristics of these A_3BX_6 (Ag_3BiI_6, $Ag_3BiI_3(SCN)_3$ and Cu_3BiI_6) solar cells with different structure (n-i-p and p-i-n, in Fig. 1) under simulated irradiation of 1 SUN are shown in Fig. 8, which were the I–V curves for the best PCE in the series. The photovoltaic parameters were summarized in Table 14. Basically, *V*oc using porous-TiO_2 layer were higher than using planer-NiO one. The effect of hysteresis on NiO layer was larger, which were different from $A_3B_2X_9$ [$(CH_3NH_3)_3Bi_2I_9$, $(CH_3NH_3)_3Sb_2I_9$, and $(CH_3NH_3)_3SbBiI_9$] solar cells (Fig. 5). But, specially, the cells using Ag_3BiI_6 on NiO and $Ag_3BiI_3(SCN)_3$ on TiO_2 perform the strong hysteresis and large overshooting at the reverse voltage scanning, which is the overestimation of photovoltaic results. The best J_{SC} and PCE in this work using trivalent B-site cation crystals are shown in Fig. 8a with the cell configuration of <FTO/cp-TiO_2/mp-TiO_2/Ag_3BiI_6/spiro-OMeTAD/Au>. Although there was the hysteresis, the variation was not large as other combinations. The observed PCE (reverse scan) of Ag_3BiI_6 based photon harvesting layer attained 1.08% (Fig. 8a, Table 14), which is comparable of reported PCE using $AgBi_2I_7$ based photo absorber [32]. This relatively-high PCE would be due to the pinhole-less surface morphology. However, the association of Ag_3BiI_6 layer in inverted architecture could result in only 0.32% PCE (Fig. 8b and Table 14). The IPCE of the Ag_3BiI_6 based mesoscopic solar cell is shown in Fig. 8g, the close matching of Jsc of 1.78 mA cm^{-2} is observed. We tried to measure the IPCE of other lead free solar cell, but IPCE measurements could not be managed due to the low J_{SC} values. It was interesting that there was negligible hysteresis at the photo I–V measurements of <FTO/cp-TiO_2/mp-TiO_2/Cu_3BiI_6/spiro-OMeTAD/Au> cells, which would have the significance for the further research efforts in the future.

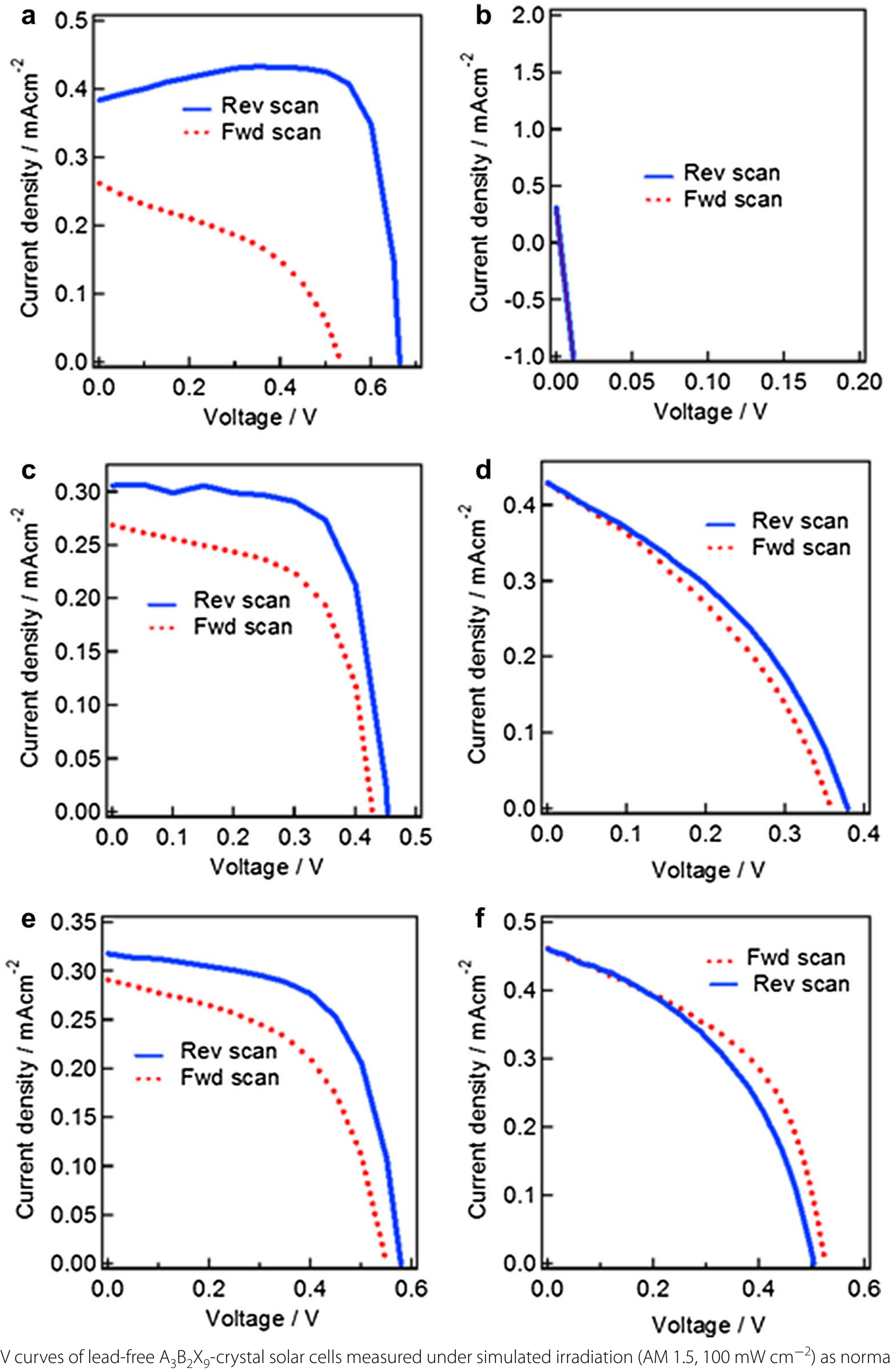

Fig. 5 Photo I–V curves of lead-free $A_3B_2X_9$-crystal solar cells measured under simulated irradiation (AM 1.5, 100 mW cm^{-2}) as normal mesoscopic and inverted architectures respectively. The photoabsorption layers were $(CH_3NH_3)_3Bi_2I_9$ (**a**, **b**), $(CH_3NH_3)_3Sb_2I_9$ (**c**, **d**), and $(CH_3NH_3)_3SbBiI_9$ (**e**, **f**) crystal films. The photovoltaic characteristics were summarized in Table 7

Table 7 Photovoltaic performance of $(CH_3NH_3)_3Bi_2I_9$, $(CH_3NH_3)_3Sb_2I_9$, $(CH_3NH_3)_3SbBiI_9$ photon harvesting layer based mesoscopic normal and inverted planar architecture solar cells

Photo-layer	Architecture	Scan direction	Efficiency/%	Jsc/mAcm^{-2}	Voc/V	FF
$(CH_3NH_3)_3Bi_2I_9$	Normal	Rev	0.21 (0.22)	0.40 (0.38)	0.64 (0.68)	0.81 (0.88)
		Fwd	0.07 (0.06)	0.29 (0.26)	0.53 (0.53)	0.45 (0.43)
$(CH_3NH_3)_3Bi_2I_9$	Inverted	Rev	0.00 (0.00)	0.27 (0.30)	0.00 (0.00)	–
		Fwd	0.00 (0.00)	0.22 (0.25)	0.00 (0.00)	–
$(CH_3NH_3)_3Sb_2I_9$	Normal	Rev	0.080 (0.095)	0.25 (0.30)	0.45 (0.45)	0.70 (0.69)
		Fwd	0.057 (0.07)	0.21 (0.26)	0.43 (0.42)	0.62 (0.61)
$(CH_3NH_3)_3Sb_2I_9$	Inverted	Rev	0.058 (0.061)	0.45 (0.43)	0.38 (0.38)	0.36 (0.37)
		Fwd	0.057 (0.055)	0.45 (0.42)	0.36 (0.35)	0.35 (0.35)
$(CH_3NH_3)_3SbBiI_9$	Normal	Rev	0.099 (0.11)	0.27 (0.31)	0.59 (0.57)	0.64 (0.62)
		Fwd	0.067 (0.084)	0.23 (0.29)	0.55 (0.54)	0.55 (0.52)
$(CH_3NH_3)_3SbBiI_9$	Inverted	Rev	0.05 (0.10)	0.44 (0.46)	0.32 (0.50)	0.34 (0.44)
		Fwd	0.06 (0.11)	0.44 (0.46)	0.34 (0.52)	0.35 (0.47)

Data shown here represent the average of three independent solar cell parameters. Best representative photovoltaic parameters are shown in the bracket

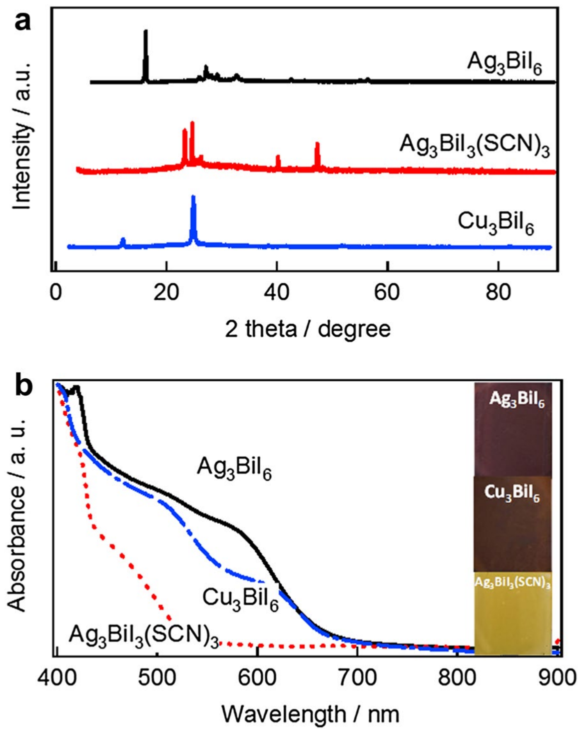

Fig. 6 XRD patterns (**a**) and UV–vis absorption spectra (**b**) of Ag_3BiI_6, $Ag_3BiI_3(SCN)_3$ and Cu_3BiI_6 casted on the glass substrates. The insets were the pictures of Ag_3BiI_6, $Ag_3BiI_3(SCN)_3$ and Cu_3BiI_6 films

3 Conclusions

In summary, we fabricated the lead-free hybrid solar cells in standard mesoscopic and inverted architecture incorporating various solution processed photon harvesting layer of $(CH_3NH_3)_3Bi_2I_9$, $(CH_3NH_3)_3Sb_2I_9$, $(CH_3NH_3)_3SbBiI_9$, Ag_3BiI_6, $Ag_3BiI_3(SCN)_3$ and Cu_3BiI_6. The best PCE results was obtained using <FTO/cp-TiO_2/mp-TiO_2/Ag_3BiI_6/spiro-OMeTAD/Au> structure with 1.08% of power conversion efficiency (PCE). The grown morphology of $A_3B_2X_9$ and A_3BX_6 crystals can be different on the substrates (porous TiO_2 or planar NiO layers). The unevenness can be the hindrance for the improvement of photovoltaic effects. Hence, it is advisable to use lead-free element which can show uniform coverage of the substrate.

Other interesting findings in this report were the prohibition of short circuiting of solar cells using Sb deposition on NiO layer and the diminishment of photo I–V hysteresis using porous-TiO_2/Cu_3BiI_6 combination, which can be considered for the further progresses.

4 Experimental details

All chemicals were of reagent grade quality and used without any further processing. Antimony iodide (SbI_3) was purchased from Yanagishima Pharmaceutical Co. Ltd. Bismuth iodide (BiI_3), Silver iodide (AgI), Nickel (II) acetylacetonate, Phenyl-C61-butyric acid methyl ester (PCBM) and bathocuproine (BCP) were purchased from Aldrich. Copper(I) iodide (CuI) from Kanto Chemical Ltd., Silver thiocyanate (AgSCN) from Wako Pure Chemical Industries Ltd., and Methylammonium iodide was purchased from TCI respectively. Dimethyl sulfoxide (DMSO), Chlorobenzene, and Methanol were purchased from Wako. γ-Butyrolactone (GBL) and Acetonitrile were procured from Chameleon Reagent and Kanto Chemical Co. Inc. respectively.

FTO glass (TEC-15, t = 2.1 mm), purchased from Pilkington were cut in an appropriate size and cleaned ultrasonically with detergent water, distilled water and ethanol, respectively each for 15 min. The cleaned FTO

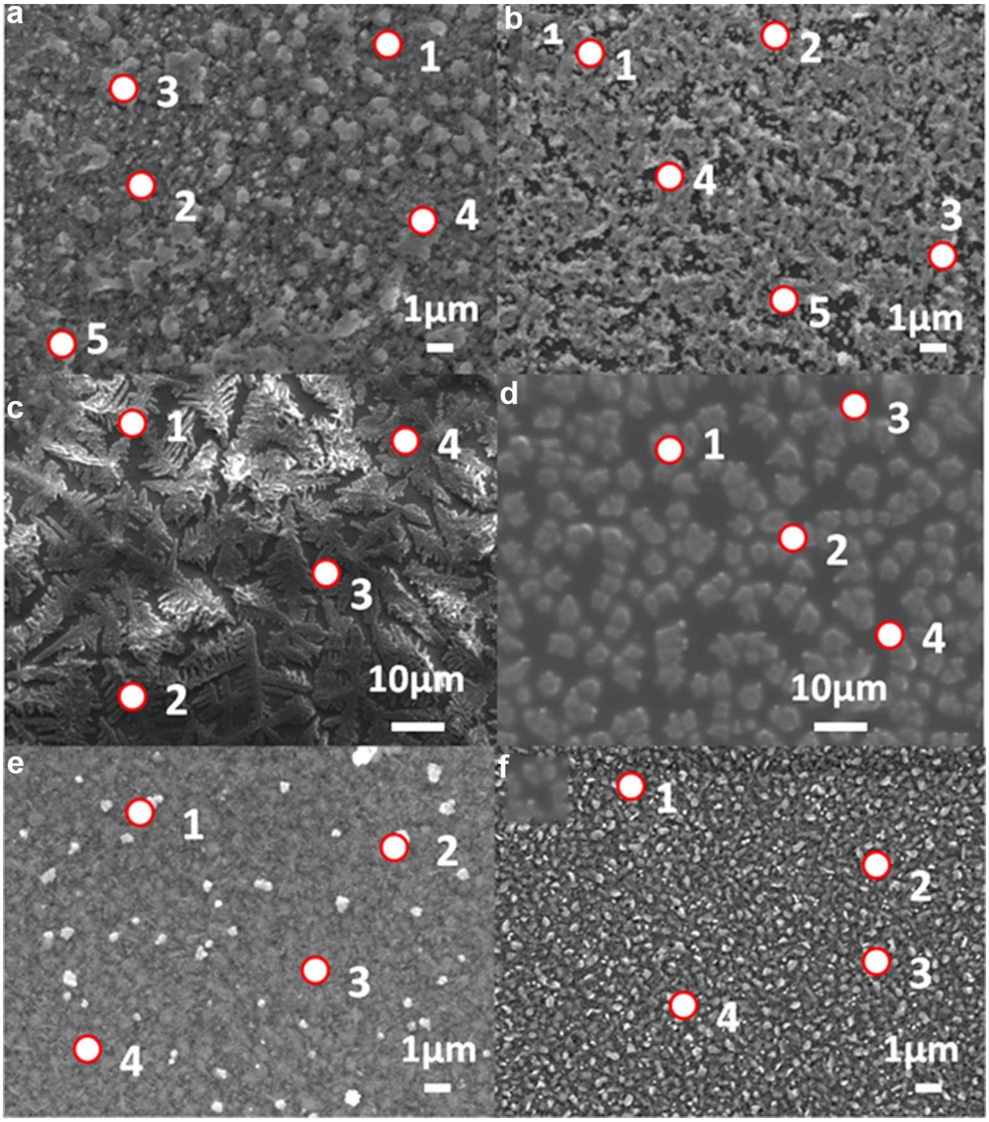

Fig. 7 SEM images observed for elemental analysis of A_3BX_6 films [Ag_3BiI_6: (**a**, **b**); $Ag_3BiI_3(SCN)_3$: (**c**, **d**); Cu_3BiI_6: (**e**, **f**)] grown on different substrates [TiO_2: (**a**, **c**, **e**); NiO: (**b**, **d**, **f**)]. The marked spots indicate the positions of elemental analysis, which is related to the results shown in Tables 8, 9, 10, 11, 12 and 13

Table 8 Elemental distribution (atomic %) of the individual elements observed on a particular spot on Ag_3BiI_6/TiO_2 substrate shown in Fig. 8a

Spot	Bismuth	Silver	Iodine	Titanium	Oxygen	Silicon
Point 1	4.75	32.89	33.54	11.97	9.11	7.75
Point 2	2.01	65.52	16.29	7.19	5.76	3.24
Point 3	2.73	20.47	19.50	15.86	19.65	21.79
Point 4	1.80	53.99	18.38	10.09	11.56	4.18
Point 5	5.03	43.57	26.93	15.62	3.98	4.87

Table 9 Elemental distribution (atomic %) of the individual elements observed on a particular spot on Ag_3BiI_6/NiO substrate shown in Fig. 8b

Spot	Bismuth	Silver	Iodine	Nickel	Oxygen	Silicon
Point 1	2.00	32.49	10.34	1.06	14.54	39.57
Point 2	4.88	40.11	20.99	1.04	6.98	25.99
Point 3	2.87	45.38	23.67	1.10	6.98	19.99
Point 4	0.83	29.68	5.36	0.69	24.20	39.25
Point 5	0.58	89.08	4.83	0.30	3.55	1.65

Table 10 Elemental distribution (atomic %) of the individual elements observed on $Ag_3BiI_3(SCN)_3/TiO_2$ substrate shown in Fig. 8c

Spot	Bismuth	Silver	Iodine	Sulphur	Carbon	Nitrogen	Titanium	Oxygen	Silicon
Point 1	3.10	20.88	10.24	2.54	7.94	3.40	12.17	19.97	21.76
Point 2	3.31	45.94	15.54	2.72	6.08	–	11.52	8.57	6.33
Point 3	3.71	29.29	12.62	2.97	8.06	0.84	13.16	12.64	16.71
Point 4	3.98	26.85	8.77	3.29	7.04	4.89	13.25	18.52	13.40

Table 11 Elemental distribution (atomic %) of the individual elements observed on $Ag_3BiI_3(SCN)_3$/NiO substrate shown in Fig. 8d

Spot	Bismuth	Silver	Iodine	Sulfur	Carbon	Nitrogen	Nickel	Oxygen	Silicon
Point 1	3.23	7.19	13.82	5.35	19.35	4.71	0.48	25.38	20.50
Point 2	2.40	41.86	13.76	2.61	8.85	–	0.65	11.82	18.04
Point 3	0.58	16.57	0.91	0.71	10.50	–	0.79	42.75	27.19
Point 4	0.60	16.75	0.84	0.78	11.19	–	0.85	39.73	19.26

Table 12 Elemental distribution (atomic %) of the individual elements observed on Cu_3BiI_6/TiO_2 substrate shown in Fig. 8e

Spot	Copper	Bismuth	Iodine	Titanium	Oxygen	Silicon
Point 1	16.38	1.59	22.26	8.54	32.17	19.06
Point 2	9.18	1.65	17.42	9.76	37.88	24.11
Point 3	6.21	1.48	13.18	8.04	42.66	28.44
Point 4	3.20	1.90	9.40	8.35	47.70	29.45

Table 13 Elemental distribution (atomic %) of the individual elements observed on Cu_3BiI_6/NiO substrate shown in Fig. 8f

Spot	Copper	Bismuth	Iodine	Nickel	Oxygen	Silicon
Point 1	2.19	0.46	3.75	0.57	56.42	36.61
Point 2	4.18	1.03	12.15	0.71	48.00	33.92
Point 3	1.94	0.48	3.77	0.66	51.91	41.23
Point 4	3.29	1.84	7.70	0.52	52.41	34.24

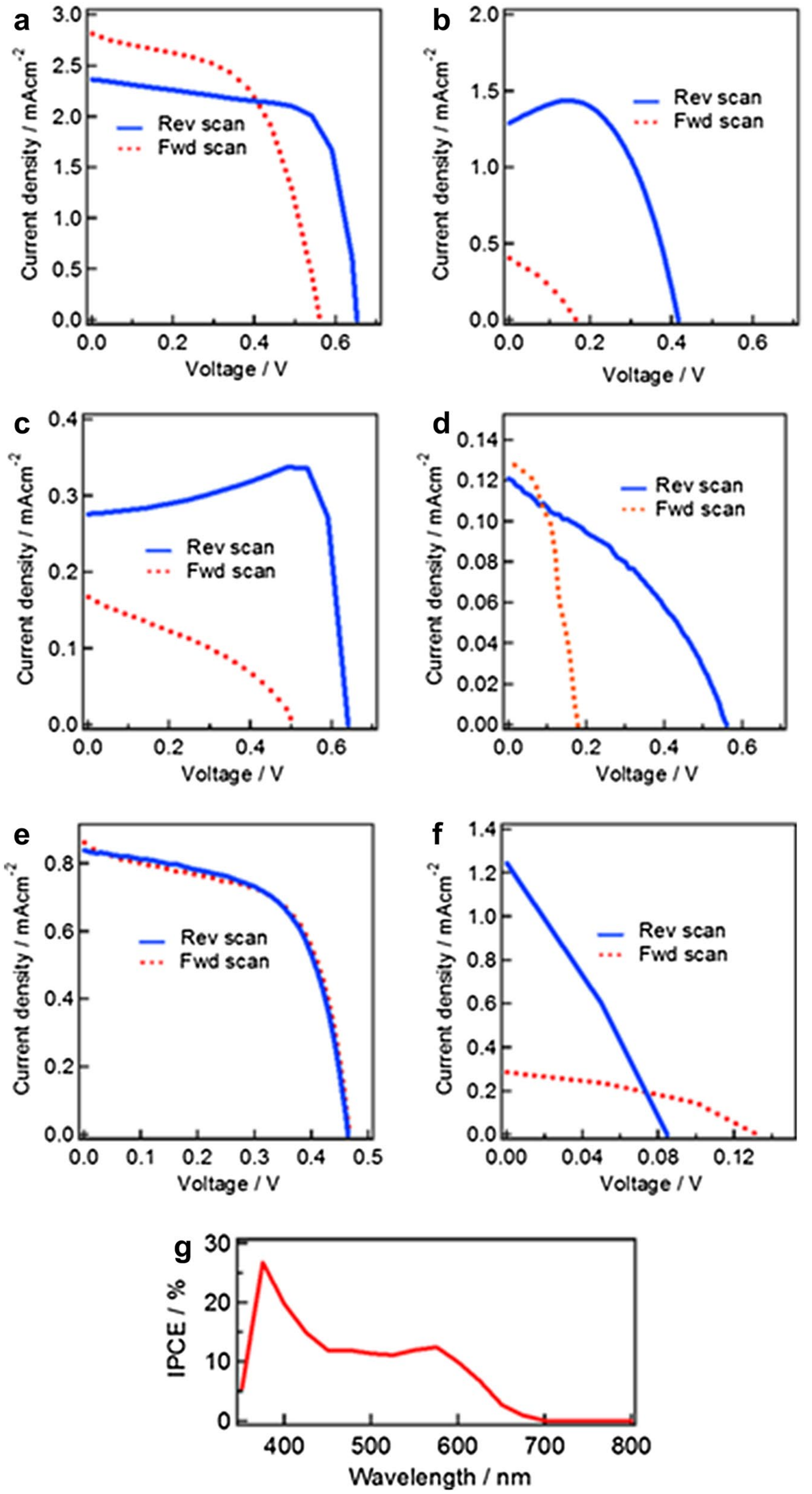

Fig. 8 Photo I–V curves of lead-free A_3BX_6-crystal solar cells measured under simulated irradiation (AM 1.5, 100 mW cm^{-2}) as normal mesoscopic and inverted architectures respectively. The photoabsorption layers are Ag_3BiI_6 (**a**, **b**), $Ag_3BiI_3(SCN)_3$ (**c**, **d**), and Cu_3BiI_6 (**e**, **f**) crystal films, and IPCE spectrum of the mesoscopic structure with the Ag_3BiI_6 layer (**g**). The photovoltaic characteristics were summarized in Table 14

Table 14 Photovoltaic performance of Ag_3BiI_6, $Ag_3BiI_3(SCN)_3$ photon harvesting layer based mesoscopic normal and inverted planar architecture solar cells (Fig. 8g)

Photo-layer	Architecture	Scan direction	Efficiency/%	Jsc/mAcm^{-2}	Voc/V	FF
Ag_3BiI_6	Normal	Rev	0.91 (1.08)	1.92 (2.36)	0.63 (0.65)	0.75 (0.70)
		Fwd	0.58 (0.88)	1.92 (2.81)	0.52 (0.56)	0.56 (0.55)
Ag_3BiI_6	Inverted	Rev	0.14 (0.32)	0.99 (1.29)	0.25 (0.41)	0.42 (0.59)
		Fwd	0.02 (0.02)	0.39 (0.40)	0.14 (0.16)	0.31 (0.32)
$Ag_3BiI_3(SCN)_3$	Normal	Rev	0.14 (0.18)	0.32 (0.27)	0.63 (0.63)	0.72 (1.00)
		Fwd	0.02 (0.03)	0.21 (0.16)	0.40 (0.50)	0.30 (0.35)
$Ag_3BiI_3(SCN)_3$	Inverted	Rev	0.007 (0.02)	0.12 (0.12)	0.17 (0.55)	0.34 (0.36)
		Fwd	0.02 (0.01)	0.11 (0.13)	0.46 (0.17)	0.42 (0.46)
Cu_3BiI_6	Normal	Rev	0.19 (0.23)	0.69 (0.83)	0.45 (0.46)	0.59 (0.60)
		Fwd	0.19 (0.23)	0.71 (0.86)	0.46 (0.46)	0.57 (0.59)
Cu_3BiI_6	Inverted	Rev	0.028 (0.03)	1.70 (1.24)	0.06 (0.08)	0.27 (0.29)
		Fwd	0.016 (0.017)	0.32 (0.28)	0.13 (0.13)	0.39 (0.45)

Data shown here represent the average of three independent solar cell parameters. Best representative photovoltaic parameters are shown in the bracket

glass was passed through UV-O_3 treatment for 10 min to remove the organic impurities. To fabricate the standard mesoscopic n-i-p solar cell, diluted TAA solution (Titanium di isopropoxide bis(acetylacetonate)/Sigma-Aldrich) of (200 μL in 7.5 mL ethanol) was aerosol spray coated maintaining the substrate temperature 500 °C. After arriving the ambient temperature the coated FTO glass was passed through the UV-O_3 treatment and, diluted PST-30NRD TiO_2 solution (1:3.5 wt/wt) was coated by spinning process at 5000 rpm for 30 s. The mesoporous TiO_2 coated substrate was dried out at 120 °C for 5 min and again baked at 500 °C for 30 min in a furnace.

To make the perovskite layer, the substrate was treated for 5 min for UV-O_3 treatment and transferred inside N_2 filled glove box. To prepare the $(CH_3NH_3)_3Sb_2I_9$ film, SbI_3 and methylammonium iodide was mixed in DMSO:GBL (1:1) solvent and 0.25 M concentration of $(CH_3NH_3)_3Sb_2I_9$ was maintained by keeping the molar ratio as $CH_3NH_3I{:}SbI_3 = 3{:}2$ molar ratio. To prepare the $(CH_3NH_3)_3Bi_2I_9$ film, BiI_3 and methylammonium iodide was mixed to maintain the 0.25 M concentration of $(CH_3NH_3)_3Bi_2I_9$ in DMSO:GBL (1:1) by keeping the molar ratio as $CH_3NH_3I{:}BiI_3 = 3{:}2$. To prepare the $(CH_3NH_3)_3SbBiI_9$ film, SbI_3, BiI_3 and methylammonium iodide was mixed to maintain the 0.25 M concentration of $(CH_3NH_3)_3SbBiI_9$ in DMSO:GBL (1:1) by keeping the molar ratio as $CH_3NH_3I{:}SbI_3{:}BiI_3 = 3{:}1{:}1$. Semiconductor Ag_3BiI_6 layer overcoated TiO_2 mp substrate was prepared by making a 0.5 M solution of AgI and BiI_3 in DMSO solvent with 0.5 M concentration of Ag_3BiI_6 by keeping the molar ratio as $AgI{:}BiI_3 = 3{:}1$. To fabricate and explore the photon harvesting properties of $Ag_3BiI_3(SCN)_3$, BiI_3 and Silver thiocyanate (AgSCN) was mixed in 1:3 molar ratio to maintain the 0.5 M concentration in DMSO solvent. Copper based photon harvesting layer (Cu_3BiI_6) was prepared by mixing the CuI and BiI_3 in DMSO solvent with 0.4 M concentration of Cu_3BiI_6 by keeping the molar ratio as $CuI{:}BiI_3 = 3{:}1$.

In all cases, the solution temperature was maintained at 80 °C and the heated solution was spun on mp TiO_2 substrate with 2000 rpm for 30 s and preserved on a hot plate at 80 °C for 30 min to grow the respective photo absorber layer.

To collect the holes smoothly a hole selective layer spiro-OMeTAD (2,2,7,7-Tetrakis(*N*,*N*di-p-methoxy phenylamine)-9,9-spirobifluorene)of 28.9 mg in 400 μL chlorobenzene, with additives [11.5 μL t-butyl pyridine (Sigma-Aldrich), 7 μL Li-TFSI (520 mg in 1 mL acetonitrile) and 8.8 μL Co Complex (40 mg in 0.1 mL acetonitrile)] was spun on a cold substrate of lead-free prepared semiconducting layer at 4000 rpm for 20 s and stored for drying under dark. Finally, gold layer was thermally evaporated and deposited to maintain 80 nm thickness, which works as a metal back contact layer.

The inverted structure hybrid solar cell was fabricated by coating Nickel (II) acetylacetonate in acetonitrile (0.04 M) solution by spray process while maintaining the UV-O_3 treated FTO glass temperature at 500 °C. After reaching the ambient temperature the coated NiO substrate was transferred to N_2 filled glove box for lead-free semiconductor layer preparation. The preparation of individual photo harvesting layer was followed as described previously. On top of the lead-free photo absorber layer, a 20 mg/mL PCBM in chlorobenzene was spun at 1000 rpm for 60 s and kept under ambient N_2 for 30 min to dry it out. Subsequently, a BCP solution of 1 mg/mL in methanol was spun at 1000 rpm for 60 s.

Finally, a silver metal contact was prepared by thermally evaporation process maintaining its thickness 80 nm.

The I–V characteristics were measured by an AM 1.5G solar simulator equipped with a 500 W Xe lamp (YSS-80A, Yamashita Denso) by placing a black 0.09 cm^2 mask area. A reference Si photodiode (Bunkou keiki co. ltd., Japan) was used to calibrate the power of the solar simulator light. The I–V characteristics were obtained by applying an external bias to the fabricated solar cell and measurement of generated photocurrent was performed with a DC voltage current source (Agilent, B2901A). SEM images were obtained by HITACHI Microscope TE3030 and EDX analysis was performed with Oxford Instruments, X-stream-2.

Authors' contributions

HM, HS performed the experiments. AKB, HM, NS analysed the data. AKB, HK, NS, and SI designed the experiments. AKB, HM, HS, HK, SK, NS, YS, MI, YN, KY, TM, TU, and HI provided an equal contribution in useful discussion and modification. AKB and SI wrote the manuscript. All authors read and approved the final manuscript.

Author details

[1] Department of Materials and Synchrotron Radiation Engineering, Graduate School of Engineering, University of Hyogo, 2167 Shosha, Himeji, Hyogo 671-2280, Japan. [2] Graduate School of Engineering, Toin University of Yokohama, Yokohama, Kanagawa 225-8503, Japan. [3] Department of Applied Molecular Chemistry, College of Industrial Technology, Nihon University, 1-2-1, Izumi-Chou, Narashino-Shi, Chiba 275-8575, Japan. [4] Department of Molecular Engineering, Graduate School of Engineering and Institute for Integrated Cell Materials Sciences (WPI-iCeMS), Kyoto University, Nishikyo-Ku, Kyoto 615-8510, Japan.

Competing interests

The authors declare that they have no competing interests.

Availability of data and materials

The authors have no any more data to share.

Consent to publication

Not applicable.

Ethics approval and consent to participate

Not applicable.

Funding and Acknowledgements

We would like to express sincere thanks to the Advanced Low Carbon Technology Research and Development Program (ALCA-JST), Japan.

Publisher's Note

Received: 15 June 2017 Accepted: 17 September 2017

References

1. A. Kojima, K. Teshima, Y. Shirai, T. Miyasaka, J. Am. Chem. Soc. **131**, 6050 (2009)
2. S. Ito, APL Mater. **4**, 91504 (2016)
3. W.S. Yang, B.-W. Park, E.H. Jung, N.J. Jeon, Y.C. Kim, D.U. Lee, S.S. Shin, J. Seo, E.K. Kim, J.H. Noh, S. Il Seok, Science **356**, 1376 (2017)
4. T.A.N. Peiris, A.K. Baranwal, H. Kanda, S. Fukumoto, S. Kanaya, L. Cojocaru, T. Bessho, T. Miyasaka, H. Segawa, S. Ito, Nanoscale **9**, 5475 (2017)
5. A.K. Baranwal, S. Kanaya, T.A.N. Peiris, G. Mizuta, T. Nishina, H. Kanda, T. Miyasaka, H. Segawa, S. Ito, Chemsuschem **9**, 2604 (2016)
6. S. Ito, G. Mizuta, S. Kanaya, H. Kanda, T. Nishina, S. Nakashima, H. Fujisawa, M. Shimizu, Y. Haruyama, H. Nishino, Phys. Chem. Chem. Phys. **18**, 27102 (2016)
7. S. Bae, S. Kim, S.-W. Lee, K.J. Cho, S. Park, S. Lee, Y. Kang, H.-S. Lee, D. Kim, J. Phys. Chem. Lett. **7**, 3091 (2016)
8. A. Babayigit, A. Ethirajan, M. Muller, B. Conings, Nat. Mater. **15**, 247 (2016)
9. S.F. Hoefler, G. Trimmel, T. Rath, Monatsh. Chem. **148**, 795 (2017)
10. E.S. Parrott, R.L. Milot, T. Stergiopoulos, H.J. Snaith, M.B. Johnston, L.M. Herz, J. Phys. Chem. Lett. **7**, 1321 (2016)
11. F. Hao, C.C. Stoumpos, D.H. Cao, R.P.H. Chang, M.G. Kanatzidis, Nat. Photonics **8**, 489 (2014)
12. A. Babayigit, D. Duy Thanh, A. Ethirajan, J. Manca, M. Muller, H.-G. Boyen, B. Conings, Sci. Rep. **6**, 18721 (2016)
13. T. Krishnamoorthy, H. Ding, C. Yan, W.L. Leong, T. Baikie, Z. Zhang, M. Sherburne, S. Li, M. Asta, N. Mathews, S.G. Mhaisalkar, J. Mater. Chem. A **3**, 23829 (2015)
14. D. Cortecchia, H.A. Dewi, J. Yin, A. Bruno, S. Chen, T. Baikie, P.P. Boix, M. Grätzel, S. Mhaisalkar, C. Soci, N. Mathews, Inorg. Chem. **55**, 1044 (2016)
15. S. Öz, J.-C. Hebig, E. Jung, T. Singh, A. Lepcha, S. Olthof, F. Jan, Y. Gao, R. German, P.H.M. van Loosdrecht, K. Meerholz, T. Kirchartz, S. Mathur, Sol. Energy Mater. Sol. Cells **158**, 195 (2016)
16. J.-C. Hebig, I. Kühn, J. Flohre, T. Kirchartz, A.C.S. Energ, Lett. **1**, 309 (2016)
17. B.W. Park, B. Philippe, X. Zhang, H. Rensmo, G. Boschloo, E.M.J. Johansson, Adv. Mater. **27**, 6806 (2015)
18. A. Kulkarni, T. Singh, M. Ikegami, T. Miyasaka, RSC Adv. **7**, 9456 (2017)
19. T. Singh, Y. Udagawa, M. Ikegami, H. Kunugita, K. Ema, T. Miyasaka, APL Mater. **5**, 16103 (2017)
20. G. Volonakis, A.A. Haghighirad, R.L. Milot, W.H. Sio, M.R. Filip, B. Wenger, M.B. Johnston, L.M. Herz, H.J. Snaith, F. Giustino, J. Phys. Chem. Lett. **8**, 772 (2017)
21. G. Volonakis, M.R. Filip, A.A. Haghighirad, N. Sakai, B. Wenger, H.J. Snaith, F. Giustino, J. Phys. Chem. Lett. **7**, 1254 (2016)
22. E.T. McClure, M.R. Ball, W. Windl, P.M. Woodward, Chem. Mater. **28**, 1348 (2016)
23. I. Turkevych, S. Kazaoui, E. Ito, T. Urano, K. Yamada, H. Tomiyasu, H. Yamagishi, M. Kondo, S. Aramaki, Chemsuschem **8575**, 1 (2017)
24. H.C. Sansom, G.F.S. Whitehead, M.S. Dyer, M. Zanella, T.D. Manning, M.J. Pitcher, T.J. Whittles, V.R. Dhanak, J. Alaria, J.B. Claridge, M.J. Rosseinsky, Chem. Mater. **29**, 1538 (2017)
25. F. Wei, Z. Deng, S. Sun, F. Zhang, D.M. Evans, G. Kieslich, S. Tominaka, M.A. Carpenter, J. Zhang, P.D. Bristowe, A.K. Cheetham, Chem. Mater. **29**, 1089 (2017)
26. H.-S. Kim, J.-Y. Seo, N.-G. Park, J. Phys. Chem. C **120**, 27840 (2016)
27. H.-S. Kim, J.-Y. Seo, N.-G. Park, Chemsuschem **9**, 2528 (2016)
28. M. Saliba, J.-P. Correa-Baena, M. Graetzel, A. Hagfeldt, A. Abate, Angew. Chemie Int. Ed. (2017). doi:10.1002/anie.201703226
29. G. Murugadoss, G. Mizuta, S. Tanaka, H. Nishino, T. Umeyama, H. Imahori, S. Ito, APL Mater. **2**, 81511 (2014)
30. H.-S. Kim, I.-H. Jang, N. Ahn, M. Choi, A. Guerrero, J. Bisquert, N.-G. Park, J. Phys. Chem. Lett. **6**, 4633 (2015)
31. T. Oldag, T. Aussieker, H.-L. Keller, C. Preitschaft, A. Pfitzner, ChemInform **36**, 44227 (2005)
32. Y. Kim, Z. Yang, A. Jain, O. Voznyy, G.-H. Kim, M. Liu, L.N. Quan, F.P. García de Arquer, R. Comin, J.Z. Fan, E.H. Sargent, Angew. Chemie Int. Ed. **55**, 9586 (2016)